Journal of Hydrology 568 (2019) 12–25

Contents lists available at ScienceDirect

Journal of Hydrology

journal homepage: www.elsevier.com/locate/jhydrol

Research papers

Variability, teleconnection, and predictability of Korean precipitation in relation to large scale climate indices

Jai Hong Lee[a,*], Jorge A. Ramirez[b], Tae Woong Kim[c], Pierre Y. Julien[b]

[a] Department of Civil and Mechanical Engineering, South Carolina State University, Orangeburg, SC 29117, USA
[b] Department of Civil and Environmental Engineering, Colorado State University, Fort Collins, CO 80523, USA
[c] Department of Civil and Environmental Engineering, Hanyang University, Ansan 426-791, South Korea

ARTICLE INFO

This manuscript was handled by Dr. A. Bardossy, Editor-in-Chief, with the assistance of Alessio Domeneghetti, Associate Editor

Keywords:
Precipitation variability
Teleconnection
El Niño Southern Oscillation

ABSTRACT

Spatiotemporal variability, teleconnection, and predictability of the Korean precipitation related to large scale climate indices were examined based on leading patterns of observed monthly Rx5day and total precipitation through an empirical orthogonal teleconnection (EOT). Cross-correlation and lag regression analyses for the leading modes and global atmospheric circulation dataset were employed on a monthly basis. The spatial pattern of the leading EOT modes for Rx5day and total precipitation represents a northern inland mode for boreal summer and a southern coastal mode in boreal winter. The temporal evolution of the leading EOT modes exhibits increasing trends during summer season and decadal variability for winter season. The leading EOT patterns of Rx5day precipitation show more widespread coherent patterns than those of total precipitation during warm and cold seasons, while the former explains less variance in precipitation variability than the latter. The tropical ENSO forcing has a coherent teleconnection with September and November-December precipitation patterns, while the Indian Ocean dipole is identified as a driver for precipitation variability in September and November. The monsoon circulation over the western North Pacific also exhibits a significant negative correlation with winter precipitation EOTs, while tropical cyclone indices are positively correlated with the fall precipitation EOTs. The leading patterns of the September and December Rx5day precipitation time series are predictable at up to six month lead time from the tropical Pacific sea surface temperatures (SSTs), while a somewhat weak predictable response from Indian Ocean SSTs was only detected at longer lead times. In addition, predictability from the Pacific SSTs for above normal precipitation is greater than that for below normal precipitation.

1. Introduction

Deciphering the physical mechanisms through which the large scale climate phenomena affect hydroclimatic processes is of great interest. The Korean peninsula experiences a large degree of spatiotemporal precipitation variability. Precipitation varies with fluctuation of various global-regional scale climate indices (CIs) including the El Niño–Southern Oscillation (ENSO), Indian Ocean dipole (IOD), western North Pacific monsoon, and tropical cyclone activity. These large scale climate indicators have been extensively studied because the extreme phases of these indicators can produce major hydrologic extremes of floods and droughts in many regions all over the globe. In global and regional scale studies, significant relationships have been reported between the large-scale CIs and hydro-meteorological variables such as precipitation, temperature, and streamflow in the tropics and extratropics.

The effects of the ENSO on precipitation variability on a global and regional scale have been widely documented. Since the first investigation of Walker (1923) on the influence of the Southern Oscillation (SO) on rainfall fluctuations in Indian monsoon, many recent global scale studies have documented climatic links between ENSO tropical ocean sea surface temperature variability and global precipitation anomaly patterns (e.g. Bradley et al. (1987); Kiladis and Diaz (1989); Ropelewski and Halpert (1989)). In addition, regional scale studies in low and middle latitudes (e.g. Douglas and Englehart (1981), Shukla and Paolino (1983), Kahya and Dracup (1994), Rasmusson and Wallace (1983), Redmond and Koch (1991), Price et al. (1998), Kug et al. (2010), Yeh et al. (2017), Mehr et al. (2017), Nourani et al. (2017), and Degefu and Bewket (2017)) have revealed statistically significant correlations between regional precipitation and ENSO forcing. Douglas and

* Corresponding author.
E-mail address: june.lee@colostate.edu (J.H. Lee).

https://doi.org/10.1016/j.jhydrol.2018.08.034
Received 18 April 2018; Received in revised form 31 July 2018; Accepted 15 August 2018
Available online 05 October 2018

Englehart (1981) revealed that the southeastern United States has a tendency for positive winter precipitation anomalies for the warm phase of ENSO event. Karabörk and Kahya (2003) investigated the statistically significant correlation between two opposite phases of ENSO and precipitation patterns over Turkey using harmonic analysis, and showed the mid-latitude precipitation responses to the ENSO forcing are detectable in the climate of two core regions in Turkey.

The IOD is considered one of the key CIs of precipitation variability in the Indian and Pacific rim countries. Some studies of IOD have noted the distinct behavior of the IOD-related precipitation anomalies relative to ENSO and other phenomena. Since Saji et al. (1999) reported a dipole mode of the Indian Ocean influencing precipitation fluctuations, Ashok et al. (2001, 2003) revealed that a significant statistical relationship exists between the IOD and the Indian monsoon precipitation variability as well as examined the remote response of Australian precipitation anomalies in winter to the IOD through an atmospheric general circulation model (AGCM). The monsoon activity could also be considered as a CI for precipitation variability in the Indian and Pacific rim countries. Wang et al. (2008) performed a comparative analysis on pros and cons of 25 existing East Asian monsoon indicators from a viewpoint of interannual variabilities of precipitation and circulation, suggested a new index extracted by principal component analysis, and then stressed the important role of the precipitation during the mei-yu season in quantifying the intensity of the East Asian monsoon activity.

Several recent studies for the Korean peninsula have also suggested statistically significant responses of precipitation variability to large scale CIs. Lee and Julien (2015, 2016) revealed that cold and warm ENSO phases are the dominant drivers of precipitation and temperature fluctuations over the Korean peninsula based on harmonic and lag correlation analysis. In the study on prediction of Korean precipitation variability using the downscaling super ensemble method, Kim et al. (2004) suggested that during winter precipitation variability is correlated with the second Empirical Orthogonal Function (EOF) mode of sea level pressure (SLP) over East Asia modulating moist flow from the Western North Pacific (WNP), and highlighted enhanced climatic response of the East Asian monsoon activity to precipitation anomalies in winter. Moon et al. (2005) examined the climatic links between seasonal precipitation and global Sea Surface Temperature (SST) based on the principal components extracted by independent component analysis combined with wavelet transform. They noted interannual-inderdecadal variation and increasing trend during the spring and summer seasons showing the consistent precipitation-related SST signals over Indian and Pacific Oceans. Cha (2007) investigated the relationship between ENSO and IOD mode events and the impacts of these two phenomena on the precipitation of the Korean peninsula, and indicated that the distribution of the Indian Ocean SST represents the Southern and Northern Oscillation in ENSO year, and Eastern and Western in IOD year with above normal precipitation departure in both summer and winter seasons. Also, Kim et al. (2012) carried out an exploratory analysis on the correlation of the Pacific Japan pattern with typhoon activity associated with extreme precipitation variability for all river basins in Korea, and revealed that the Tropical Cyclone (TC) activity occurs more frequently during positive Pacific Japan (PJ) phase years than negative phase years.

As described above, almost all aforementioned regional and global approaches concentrate on monthly or seasonal mean based precipitation variations, and relatively little attention has been given to the far reaching effects of climate indicators on extreme precipitation variability. Since localized and intensified extreme precipitation events have a critical effect on people's livelihood and the environment, understanding the underlying regional impacts of various climate indicators on extreme precipitation may provide a promising way to predict and respond unexpected natural hazards. Also, the previous studies have focused mostly on the global scale remote influences of large-scale modes of climate variability through perturbations to the large scale ocean-atmospheric circulation and less on the influence of both global and regional CIs on regional and local scale precipitation. Hence, there has been less focus in the literature concerning the climate impacts of both global and regional CIs on precipitation variability. However, the influence of CIs on the East Asian climatology is not limited to the global scale remote CIs, highlighting a gap in knowledge that requires the need for more information about the overall features of the hydrometeorological impacts modulated by various CIs. Thus, it is necessary to investigate systematically how both global and regional CIs affect extreme and total precipitation variability in East Asian regions. In the super-ensemble prediction analysis, Kim et al. (2004) revealed strong and consistent climatic link between monsoon activity and Korean precipitation variability. From the visual inspection of the station location map in their papers, a significant CI-precipitation relationship over East Asia cannot be completely discerned because of station coverage limitations. In the present study, we are motivated to expand on previous work by diagnosing the influences of global and regional CIs on precipitation variability over the Korean peninsula using an expanded surface dataset that can resolve local and regional features.

In this study, for the purpose of investigating spatiotemporal patterns of Rx5day and total precipitation over the Korean peninsula, we employed Empirical Orthogonal Teleconnection (EOT) decomposition technique, rather than the classical approach by Empirical Orthogonal Function (EOF) analysis because EOTs provide a straightforward interpretation of patterns within data with a minimum of computation. King et al. (2014) examined Australian monthly precipitation variability through EOT decomposition analysis, and found that the first December EOT mode shows notable predictability up to several month (one year) in advance given knowledge of tropical Pacific Ocean (Indian Ocean) SST. Also, in a diagnostic study to understand the physical mechanism behind the effects of large-scale climate indices on precipitation patterns in Queensland, Australia, Klingaman et al. (2013) used EOT decomposition to identify remote and local drivers affecting the inter-annual and decadal variability of seasonal precipitation patterns.

The present study mainly aims to investigate the spatial pattern and temporal behavior of Rx5day and total precipitation anomalies over the Korean peninsula through an empirical orthogonal teleconnection (EOT) decomposition method (Van den Dool et al., 2000), to identify significant teleconnections between these leading EOT modes of Korean precipitation variability and climate indicators that represent large scale climate fluctuations and regional synoptic circulations, and to demonstrate the predictability of Rx5day and total precipitation patterns through knowledge of sea surface temperature (SST) anomalies, using regression of the EOT modes onto the SST fields at varying lead times.

2. Data

The monthly precipitation gridded dataset was derived from station-based observed precipitation data covering the entire Korean peninsula. The observational data were obtained from Korea Meteorological Administration (KMA), an affiliated organization of the Ministry of Environment (MOE). The total precipitation timeseries cover more than 20 ENSO events spanning the time period 1904 through 2015. The observational records are selected only if they have less than a month missing data, and each monthly precipitation data record is required to cover at least 43 years of observation between the years 1973 and 2015, thus spanning at least 10 ENSO episodes. Using these criteria, 60 stations were used in our analysis as shown in Fig. 1. In order to estimate high resolution precipitation with a regular spaced grid, the Parameter-elevation Regression on Independent Slope Model (PRISM) developed by Daly et al. (1994, 2008) was employed for the observational precipitation data. PRISM method is well suited to regions with mountainous terrain because it incorporates a conceptual framework that addresses the spatial scale and pattern of orographic precipitation using

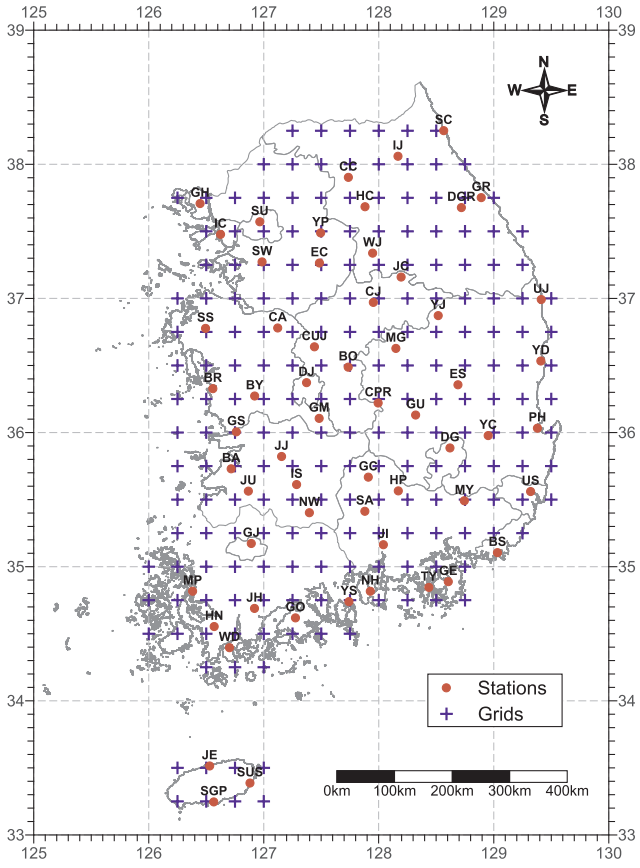

Fig. 1. Gridded precipitation data with stations.

geographic information of the elevation, distance, topographic facet, and coastal proximity (Daly et al., 2008). This model is an independent model for each target grid which can estimate target grid value by weighting each station differently based on the similarity in elevation, distance, topographic facet, and coastal proximity between observational station and target grid. Using this method, we produced grid data (0.25° × 0.25° [27.7 km × 22.2 km]) of Rx5day and total precipitation on a monthly basis from 1973 to 2015.

For comparative analysis between large scale climate indicators and precipitation EOT patterns, several CIs were applied in this present study. Taking into account both atmospheric and oceanic fluctuations, we employed the Oceanic Niño Index (ONI) and the Multivariate ENSO Index as indicators for tropical ENSO forcing, in addition to the SOI that is widely used in atmospheric circulation analysis. The ONI is one of the main indicators for monitoring the tropical ENSO phenomena. The positive phase of ENSO is represented by the condition that the ONI index exceeds +0.5, while the negative phase of ENSO is represented when the ONI index is less than −0.5. The ONI is extracted by calculating the moving average of consecutive 3-month SSTs over the east-central Pacific Ocean, also known as Niño 3.4 index area of 120–170°W and 5°S–5°N. The monthly ONI time series applied in this analysis was derived from the SST dataset of the National Oceanic Atmospheric Administration (NOAA)-Climate Prediction Center (CPC). The Multivariate ENSO Index (MEI) is derived from the leading modes calculated by unrotated decomposition technique for several air-sea variables over the tropical Pacific Ocean, including SST, Sea Level Pressure (SLP), surface air temperature, cloudiness fraction, and zonal-meridional surface wind (NOAA-Earth System Research Laboratory, Physical Sciences Division). Because it integrated both atmospheric and oceanic factors related to ENSO, the MEI may be considered as a better indicator of ENSO relative to other single variable CIs. In this analysis, we employed the standardized bimonthly MEI values regularly updated by the Climate Diagnostic Center (CDC) that start in December 1949-January 1950. The SOI, as an atmospheric pressure-based climate indicator, is usually computed using the Darwin-Tahiti Mean Sea Level Pressure (MSLP) difference based on standardized Darwin SLPs and standardized Tahiti SLPs. In the present analysis, we used the dataset of SOI calculated by the NOAA-Climate Prediction Center. Unlike the ONI and MEI, the positive phase of the SOI represents La Niña-like conditions. As an indicator of the IOD, we employ the Dipole Mode Index (DMI) computed by the empirical approach by Saji et al. (1999). This index that we obtain from the NOAA Climate Prediction Center represents the magnitude of the anomalous SST gradient from the southeastern (90–110°E, 10°S–0°) to the western (50–70°E, 10°S–10°N) near-equatorial Indian Ocean and is derived from the Hadley Centre Global Sea Ice and SST (HadISST) dataset. In the current analysis, the DMI index was employed in cross-correlation analysis as well as partial correlation analysis with the EOT time series to remove the linear influence of the ENSO forcing on precipitation variability.

To examine the relationship between the previously introduced CIs and the EOT modes for Rx5day and total precipitation, we employ SST and atmospheric circulation datasets. For SST data, the Extended Reconstructed SST (ERSST.v4) datasets (Huang et al., 2014) are used in this study. The ERSST is a global monthly SST dataset calculated based on the International Comprehensive Ocean and Atmosphere Dataset (ICOADS), which is widely used in global and regional scale studies. It is provided on a 2.0° × 2.0° grid that uses statistical techniques to provide global coverage and spans the period from January 1854 to the present. The global atmospheric circulation fields are obtained from the reanalysis derived from the joint project of the National Centers for Environmental Prediction-National center for Atmospheric Research (NCEP-NCAR), which are available on NOAA-Earth System Research Laboratory, Physical Sciences Division. This dataset is continually updated to produce fields on a 2.5° × 2.5° grid using a state-of-the-art numerical modeling system for prediction and data assimilation with continuously entrained observations. The monthly NCEP-NCAR reanalysis dataset is available for the period from 1948 to present.

Links between precipitation EOTs and monsoon circulation variability are investigated using the WNPMI index over western North Pacific. Using the methodological approach in Wang et al. (2008), the WNPMI index is calculated based on the difference between 850 hPa zonal winds (U850) in the region 5–15°N, 100–130°E and the region 20–30°N, 110–140°E. The former region represents the intensity of the monsoon westerlies from Indochina Peninsula to the Philippines, while the latter indicates the magnitude of the easterlies over the southeastern part of the WNP subtropical anticyclone. The monthly Tropical Cyclone Index (TCI) quantifying the tropical cyclone activity is calculated based on the tropical cyclone tracks recorded by the IBTrACS (Knapp et al., 2010) and the National Typhoon Center (NTC) of KMA. For the period from 1973 through 2015, the TCI is obtained from the frequency of tropical cyclones passing through the index area as shown in Fig. 2.

3. EOT and statistical analysis

The general methodology used in this present analysis, which follows the comprehensive empirical approach by Van den Dool et al. (2000) can be briefly summarized in Fig. 3, and is described in more detail below. The first step is to convert the original data to a monthly time series, i.e., transformation of precipitation time series into Standardized Precipitation Index (SPI) for Rx5day and total precipitation. Then, EOT techniques are performed for identification of the spatio-temporal variability of Rx5day and total precipitation over the Korean peninsula. The next step is to conduct both cross correlation and linear regression analyses to quantify the teleconnection between global and regional CIs and leading EOT precipitation modes. The final step is to perform a lag regression analysis using the regression of SST data onto Empirical Orthogonal Teleconnection (EOT) modes with varying lead

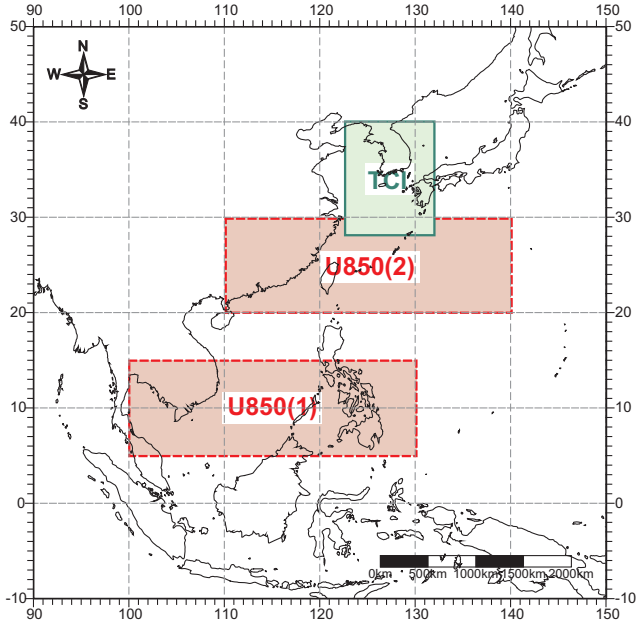

Fig. 2. Map of climate indices boundary.

times to examine the potential predictability of Rx5day and total Korean precipitation relative to Pacific tropical thermal forcing.

In this present analysis, Rx5day precipitation time series are generated following the recommendation of the Climatic Variability and Predictability (CCI/CLIVAR) panel. The monthly highest five consecutive day precipitation is employed to define Rx5day precipitation. During the period from 1973 to 2015, the monthly Rx5day and total precipitation time series are calculated for each station. Prior to the EOT analysis to examine the CI-precipitation teleconnection, we converted the precipitation data to a SPI formulated for effective assessment of wet and dry condition.

EOT analysis decomposes a SPI dataset with spatiotemporal variability into a set of orthogonal components, namely EOT patterns. The first EOT spatial modes are obtained by finding the point with the highest sum in explained variance of all other points, which is designated as a base point by Van Den Dool et al. (2000). Then, the precipitation time series of the base point is defined as the first temporal mode of the precipitation pattern. The second EOT spatial modes are extracted by removing the influence of the base point on all other points using regression analysis for precipitation time series of the base point and all other points. From this modified precipitation dataset, the second base point is identified by detecting the point explaining the most variance of the residual precipitation record. This procedure is repeated for subsequent modes until the desired number of modes is derived. The following mathematical expressions of EOT procedure are based on van den Dool et al. (2000). After detecting the base point (s_{b1}) in space that explains the maximum possible variance at all other points, its associated spatial mode, $e_1(s)$, is defined as the first EOT. The temporal mode, $\alpha_1(t)$ associated with EOT-1 is simply the original time series for its base point. After extracting EOT-1, the data are split into a portion of which variance is explained, $P_e(s, t)$ and a residual, $P_r(s, t)$ as follows.

$$P_e(s, t) = \alpha_1(t) e_1(s)$$

$$P_r(s, t) = P(s, t) - P_e(s, t)$$

where,

$$\alpha_1(t) = P(s_{b1}, t)$$

$$e_1(s) = \frac{\frac{1}{n_t}\sum_{t=1}^{nt} P(s, t) P(s_{b1}, t)}{\sqrt{\frac{1}{n_t}\sum_{t=1}^{nt} P(s, t)^2} \times \sqrt{\frac{1}{n_t}\sum_{t=1}^{nt} P(s_{b1}, t)^2}} \times \frac{\sqrt{\frac{1}{n_t}\sum_{t=1}^{nt} P(s, t)^2}}{\sqrt{\frac{1}{n_t}\sum_{t=1}^{nt} P(s_{b1}, t)^2}}$$

After dividing the data into explained and residual portions, the procedure is repeated using the once reduced data. The point in space that explains the most variance at all other points in $P_r(s, t)$ becomes the base point for EOT-2. The time series connected with EOT-2 is represented by the series at its base point in the once reduced data. After removing the variance explained by EOT-2 from the data set, the

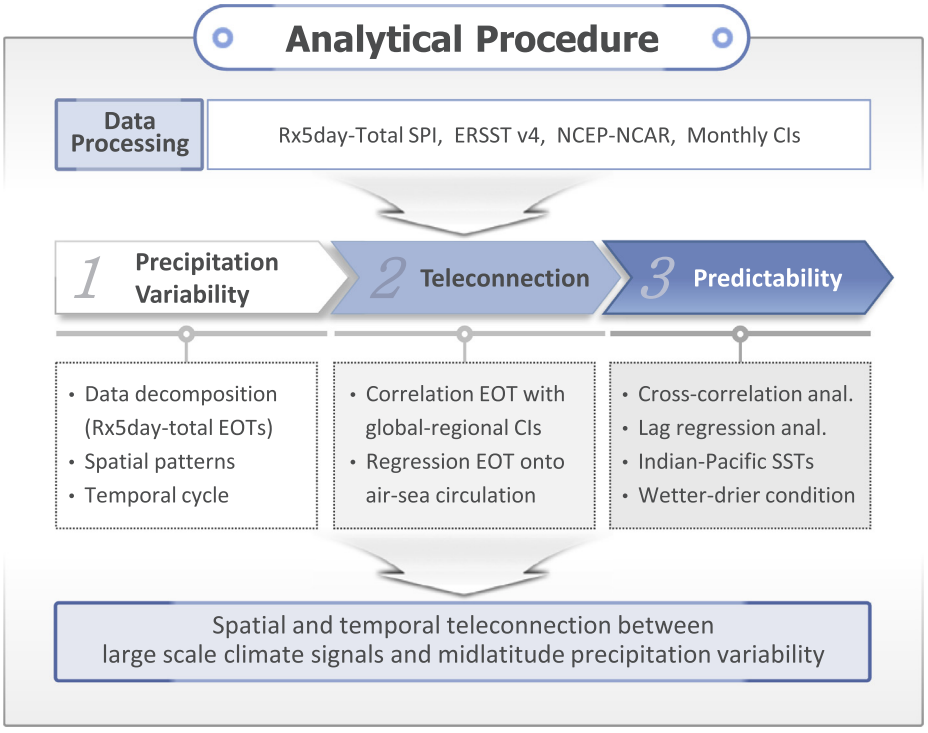

Fig. 3. Flowchart of the methodology.

process is repeated again, and so on until all of the domain variance in the original data is explained. $P_e(s, t)$ grows at the expense of $P_r(s, t)$, reordering the variance in the original data as EOT modes. The total variance (TV) in the data is expressed by,

$$TV = \frac{1}{n_t n_s} \sum_{t=1}^{n_t} \sum_{s=1}^{n_s} P(s, t)^2$$

where n_t and n_s is the numbers of points in time and space. The amount of variance explained by a particular EOT is related to the fraction of its explained variance (EV) to the total domain variance.

$$EV = \frac{\frac{1}{n_t n_s} \sum_{t=1}^{n_t} \sum_{s=1}^{n_s} P_e(s, t)^2}{TV}$$

In this analysis, we employ the revised EOT decomposition technique used by Smith (2004), who used a base point selection procedure based on the explained variance for the entire domain-weighted dataset instead of the highest sum in explained variance of all other points due to the regional biases. The first two EOT modes were selected as leading patterns of Rx5day and total precipitation variability since the subsequent EOTs after the first two EOT calculations explain less than 5% of the variance. Following the procedure above, EOT-1 and EOT-2 were obtained for monthly Rx5day and total precipitation time series during 1973–2015 to investigate patterns of precipitation fluctuations across the Korean peninsula. Due to the fact that EOT decomposition technique is orthogonal in one either space or time, while EOF is orthogonal in both space and time, EOT method provides a potentially more intuitive interpretation of the resulting patterns.

Following the approach by King et al. (2014), correlation coefficients between the precipitation EOT modes and six CIs are calculated using Spearman's correlation analysis with statistical significance assessed at the 5% level taking into account the fact that WMPMI and TCI time series do not exhibit a normal distribution. Although the correlation analysis was performed by Spearman's rank test, the resultant correlation coefficients were in general agreement with those calculated by the commonly used Pearson's correlation method (not shown here). The overall findings from correlation and regression analyses between precipitation EOT modes and various CIs are described using correlation and regression maps.

4. Results

4.1. Spatiotemporal structures of EOTs

Correlation maps for each EOT associated with the highest value of explained variance for the domain-weighted SPI were plotted for each month. The values displayed in these maps are the correlation coefficients between the precipitation EOT time series at the base point and the precipitation time series at all other points. Each leading EOT has the most explained variance for Rx5day and total precipitation. The spatial patterns of the leading EOT base points and highest correlation values for each month reflect the climatological seasonal pattern of precipitation combined with the influence of midlatitude weather systems on the Korean peninsula. The second EOT are also computed using the procedures discussed above. Fig. 4 shows the resultant patterns for the leading two EOTs of July and December Rx5day and total precipitation.

The base points of the first EOTs for Rx5day and total precipitation show different locations with respect to months. The locations of base points for Rx5day precipitation are similar to those for total precipitation during the summer months, in northern inland of the Korean peninsula. In the winter months, the base points of leading EOTs for Rx5day precipitation have a tendency to shift southward, but more so for the total precipitation time series that shifts to the southernmost island. In addition, for entire months as shown in Table 1, we categorized total EOTs into inland (north/south) and coastal (south/east) modes that take into account the locations of the base points. The centers of the Rx5day and total leading EOT modes are located in coastal area (38 modes) and inland area (10 modes). Overall, the lower-order EOT modes show more variability in the locations of the base points.

Locations of the base points indicate that out of twenty four Rx5day (total) precipitation EOTs consisting of the leading two EOTs for each of twelve months, 20 (18) are identified as coastal modes and 4 (6) are identified as inland modes as shown in Table 1. Breaking this into more detail, the coastal mode consists of an east-coast mode 8 (8) and south-coast mode 12 (10) defined on the basis of the center of leading mode. Also, the inland mode consists of the north-inland mode 3 (3) and south-inland mode 1 (3). Consistent with the patterns shown in Fig. 4, Table 1 indicates that the leading EOT modes for Rx5day and total precipitation represent a northern inland mode for boreal summer season and a southern coastal mode in winter season. In addition, more spatial homogeneity exists in both leading Rx5day and total precipitation modes during the summer than in other seasons. Summer patterns are characterized by more widespread, coherent precipitation, while in the winter season, the only leading mode of Rx5day precipitation shows nationwide spatial homogeneity.

The total spatiotemporal variance related to the two leading EOTs varies as a function of months. Table 1 shows that the spatiotemporal variance related to each Rx5day (Total) EOT mode ranges from 0.42 to 0.62 (0.49–0.68) for each first EOT mode, while that for EOT2 decreases on average to 0.14 at each month. Explained variance for the leading EOTs for total precipitation is higher than that associated with the first Rx5day precipitation EOTs in all months due to the fact that total variables are more likely to be characterized by spatially homogeneous features as opposed to Rx5day variables having more spatial incoherence (King et al., 2014).

Temporal behavior is now diagnosed for each of the EOT modes of Rx5day and total precipitation using moving average line employed by Kim et al. (2004) who defined temporal evolution of decomposed precipitation time series as increasing trend, decreasing trend, and decadal variability based on 5-year running mean plots. Also, in order to investigate the statistically significant trends in the precipitation EOT time series data, the non-parametric Mann-Kendall (MK) test and linear regression analysis are employed for the leading EOT modes considering the tests are simple and robust and can cope with missing values and values below a detection limit. Fig. 4 (lower panels) indicates time series for the leading two modes, and Table 1 summarizes behavior for all modes. For the Rx5day precipitation EOT modes, the temporal cycle showed four increasing trends, one decreasing trends, and eight decadal variabilities. The total precipitation EOT time series show eleven notable temporal patterns, including two increasing trends, two decreasing trends and seven decadal variabilities. The temporal evolution of the leading EOT modes indicates increasing trends during summer season and primarily a decadal oscillation for winter season. Specifically, the MK test statistic and p-value of summer Rx5day EOT time series are 7.43 and 0.037at the 0.05 significance level and the regression coefficient of the best fitted linear model and R-squared value are 0.036 and 0.89. Also, the MK test statistic and p-value of summer total EOT time series are 5.25 and 0.041at the 0.05 significance level and the regression coefficient and R-squared value are 0.027 and 0.65.

4.2. Teleconnections between EOTs and CIs

EOT modes were correlated with six climate indices representing spatially and temporally significant variability. We mainly discuss outcomes involving Rx5day precipitation EOTs, except where total precipitation EOTs show noticeably different results compared to those of Rx5day precipitation EOTs. The correlation coefficients of each EOT with six CIs are shown for Rx5day and total precipitation in Table 2. In addition, regression maps for NCEP-NCAR reanalysis MSLP and

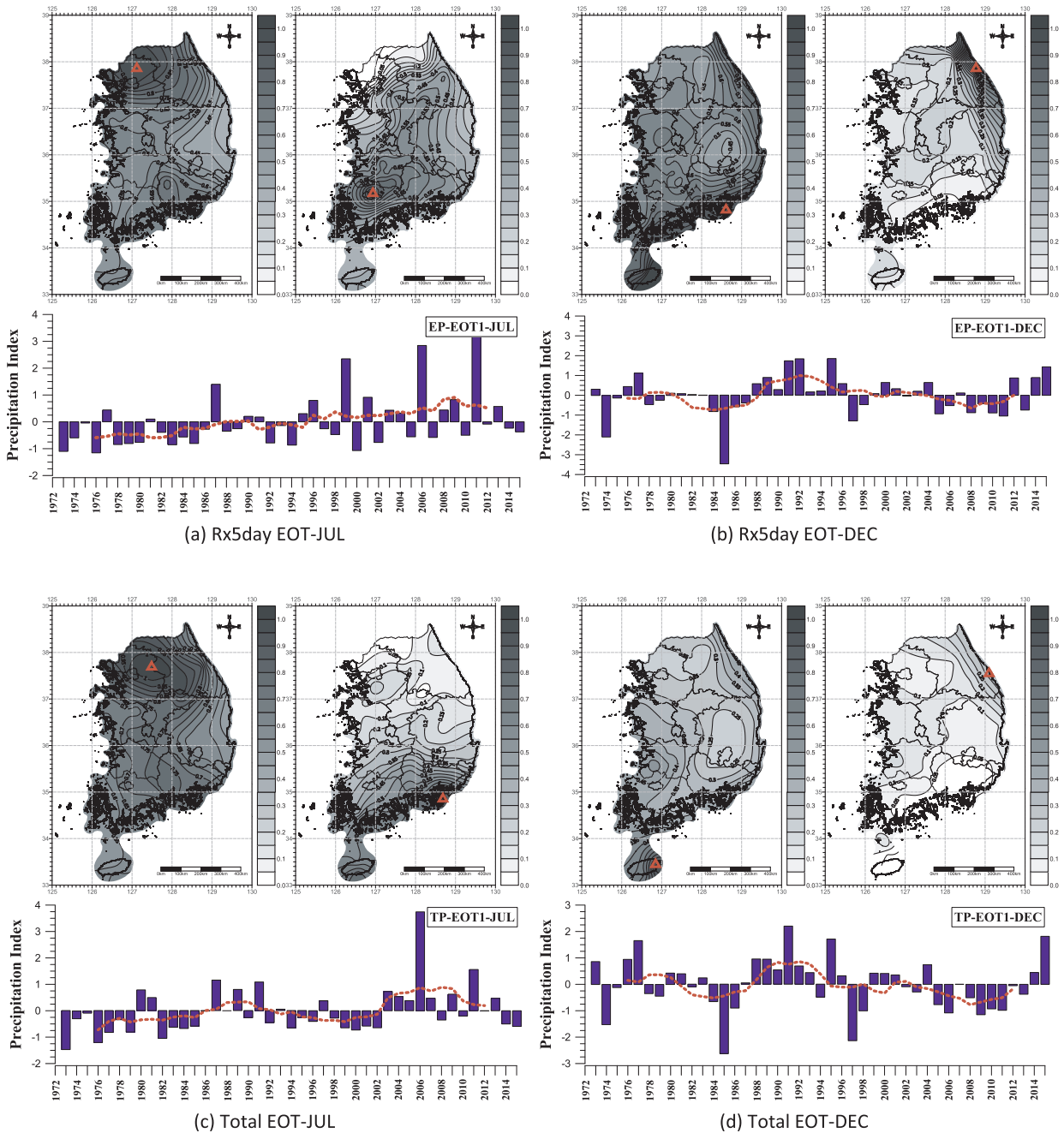

Fig. 4. Maps of the locations of base-point of each EOT and the correlations between EOT time series (i.e., base-point time series) and time series at all other points for the first-second leading EOTs of Rx5day (upper) and total (lower) precipitation. Annual time series (bars) and their 7-year running means (thick lines) for the July EOT with increasing trends (a, c), the December EOT with decadal oscillations (b, d).

ERSST.v4 SST are shown in Fig. 5 for EOT-1 during December, and maps for other modes are also discussed. Many regression maps indicate notable signals consistent with the large-scale spatial patterns reported in other studies.

The correlation coefficients for EOT-1 and EOT-2 versus the ONI, MEI, and SOI are shown in Table 2 and Fig. 6. The ONI time series has significant negative correlations with the leading EOTs for Rx5day precipitation in June and September, whereas the leading EOTs for November and December exhibit positive correlations with the tropical Pacific SST. The MEI correlations are similar to the results of ONI-related EOT signals. The SOI exhibits positive correlations with the leading Rx5day EOTs during summer season (June), while in the winter season (December) the first EOT shows significant negative correlations with the SOI. Also, the correlations are weaker in warm season than in cold season because the ENSO phenomena are generally not yet in their mature phase or are already in their decay phase. In addition to the leading EOTs, the other lower-order EOTs show relatively significant correlations in some months with ENSO indices in eastern and southern coastal areas of the Korean peninsula. The findings from the above correlation analysis suggest that the El Niño (La Niña) events make conditions more favorable for above (below) normal Rx5day precipitation in northern inland and southern coastal areas of the Korean peninsula. The total precipitation EOTs also have significant correlations with ENSO indicators. The ONI, MEI, and SOI show slightly higher correlation coefficients with the Rx5day precipitation EOTs compared with the EOT modes for total precipitation, but both correlation results show a similar seasonal cycle.

The linkages between the precipitation EOT modes and the ENSO

Table 1
Explained variance (VE) for the two leading EOT modes of monthly Rx5day and total precipitations with the center of the leading mode, which is listed in parentheses: EC (east-coast mode), SC (south-coast mode), NL (north-inland mode), SL (south-inland mode). Underlined indicates the nationwide spatial patterns. Triangles, inverted triangles, and circles indicate increasing trend, decreasing trend, and decadal variability respectively.

Mode	JAN	FEB	MAR	APR	MAY	JUN	JUL	AUG	SEP	OCT	NOV	DEC
Rx5day precipitation												
EOT-1	0.46	0.54	0.63	0.60	0.54	0.51	0.57	0.43	0.48	0.41	0.60	0.48
	(EC)	(SC)	(SC)	(SC)	(SC)	(SC)	(NL)	(NL)	(EC)	(EC)	(SC)	(SC)
		▲	▲			●	▲		●			●
EOT-2	0.22	0.18	0.17	0.18	0.21	0.22	0.19	0.25	0.23	0.25	0.15	0.20
	(SC)	(EC)	(EC)	(SC)	(SC)	(NL)	(SL)	(SC)	(SC)	(EC)	(EC)	(EC)
	●		▼	▲	●	●		●		●		
Total precipitation												
EOT-1	0.50	0.58	0.66	0.67	0.64	0.62	0.62	0.52	0.62	0.46	0.54	0.48
	(EC)	(SC)	(SC)	(SC)	(SC)	(SC)	(NL)	(NL)	(SL)	(EC)	(SC)	(SC)
			▲				▲		●			●
EOT-2	0.23	0.16	0.15	0.17	0.15	0.19	0.17	0.22	0.17	0.24	0.21	0.23
	(EC)	(EC)	(EC)	(SL)	(SC)	(NL)	(SC)	(SL)	(EC)	(SC)	(EC)	(EC)
		▼	●	▼	●			●	●	●		

indicators can also be identified through regression analysis, as shown in Fig. 5. Positive EOT precipitation modes exhibit an SST anomaly pattern consistent with a typical ENSO SST warm event, consisting of warmer SST anomalies over the central-eastern tropical Pacific and cooler SST anomalies in the western equatorial Pacific Ocean (Fig. 5a, and b). Above normal signals in many Rx5day and total precipitation EOTs are closely related to ENSO–like SST patterns. In addition to the tropical Pacific SST Pattern, regressing MSLP onto the first EOT modes for Rx5day and total precipitation (Fig. 5c and d) describes similar ENSO-like SLP patterns with higher pressure in the western North Pacific and lower pressure in the eastern North Pacific region. This pattern reflects the Pacific-East Asian teleconnection (PEA) pattern which represents a damping of the East Asian winter monsoon induced by a western North pacific anticyclone and ENSO warm phases over the eastern equatorial Pacific Ocean (Wang et al., 2000). This phase of the PEA teleconnection preferentially modulates Rx5day and total precipitation over the Korean peninsula during ENSO events.

The IOD is also associated with Rx5day and total precipitation variability in the Korean peninsula. As shown in Table 2, the leading Rx5day precipitation EOT modes are significantly correlated with the IOD as quantified by the DMI index representing the anomalous SST gradient between the western and eastern tropical Indian Ocean. The IOD time series has significant negative correlations with the leading EOTs for Rx5day precipitation in September, while the leading EOTs for November exhibit positive correlations with the tropical Indian Ocean SST. The total precipitation EOT modes also demonstrate a similar correlation with the DMI in September and November. The partial correlation of the DMI index against the EOT modes was also examined to rule out that the IOD was influencing Korean precipitation only because of its covariability with ENSO. However, the resultant numbers of significant relationships are similar to the above result, providing confidence that the IOD influences Korean precipitation in a manner independent of ENSO as reported by Saji et al. (1999).

The correlation coefficient of monsoon circulation activity with each EOT was calculated using the WNPMI index. From the results of correlation analysis in Table 2, the leading EOTs for Rx5day and total precipitation exhibit significant negative correlations with the monsoon variability over the WNP region during November and December. In the positive WNPMI phase, anomalous cyclones are reinforced in the WNP area due to the intensification of WNP monsoon trough, which is caused by the strengthening of westerlies over the U850 (1) region in Fig. 2 from the Philippine Sea to the Indochina peninsula and the enhancement of easterlies in the U850 (2) region over the southern flank of the WNP subtropical high. This positive WNPMI phase has an effect on drier than average precipitation anomaly in Korean peninsula. On the contrary, the negative WNPMI phase is associated with the reinforced anomalous anticyclones in the WNP area due to the suppression of the monsoon trough, which is caused by the weakening of westerlies over the U850 (1) region and easterlies in the U850 (2) region. The wetter than average precipitation anomaly in November and December is attributed to the negative WNPMI phase. The leading EOTs for total precipitation also show similarly significant correlation with the

Table 2
Correlation coefficients of the two leading modes with climate indicators, ONI (Oceanic Niño Index), MEI (Multivariate ENSO Index), SOI (Southern Oscillation Index), IOD (Indian Ocean Index), WNPMI (Western North Pacific Monsoon Index), and TCI (Tropical Cyclone Index). An underlined bold indicates correlations that are statistically significant at the 5% level.

Mode	CIs for Rx5day EOT modes						CIs for Total EOT modes					
	ONI	MEI	SOI	IOD	WNPMI	TCI	ONI	MEI	SOI	IOD	WNPMI	TCI
EOT-1												
JUN	**−0.38**	**−0.35**	**0.35**	−0.10	0.21	0.11	−0.24	−0.22	**0.31**	−0.14	0.23	0.20
SEP	**−0.34**	**−0.41**	**0.31**	**−0.28**	−0.24	0.16	**−0.41**	**−0.44**	0.28	**−0.27**	−0.24	**0.41**
OCT	−0.18	−0.15	0.02	−0.17	0.10	**0.38**	−0.19	−0.21	0.11	−0.10	−0.08	**0.33**
NOV	**0.33**	**0.36**	**−0.30**	**0.32**	**−0.30**	0.06	**0.39**	**0.45**	**−0.32**	**0.31**	**−0.32**	0.25
DEC	**0.49**	**0.46**	**−0.41**	0.09	**−0.37**	–	**0.45**	**0.42**	**−0.49**	−0.02	**−0.45**	–
EOT-2												
JUN	**−0.34**	0.13	−0.26	−0.04	**0.34**	−0.16	**−0.33**	−0.20	0.18	0.10	0.07	0.06
SEP	0.13	0.16	−0.04	**0.34**	0.01	−0.19	−0.13	−0.18	0.06	−0.18	0.15	0.15
OCT	**0.41**	**0.40**	**−0.40**	0.14	−0.21	0.10	**−0.30**	**−0.31**	0.10	0.01	−0.11	0.06
NOV	−0.13	−0.15	0.28	−0.16	0.08	**0.30**	−0.06	−0.06	**0.31**	−0.08	0.12	**0.31**
DEC	0.06	0.08	−0.13	0.07	−0.10	–	0.02	0.02	0.06	0.01	**0.35**	–

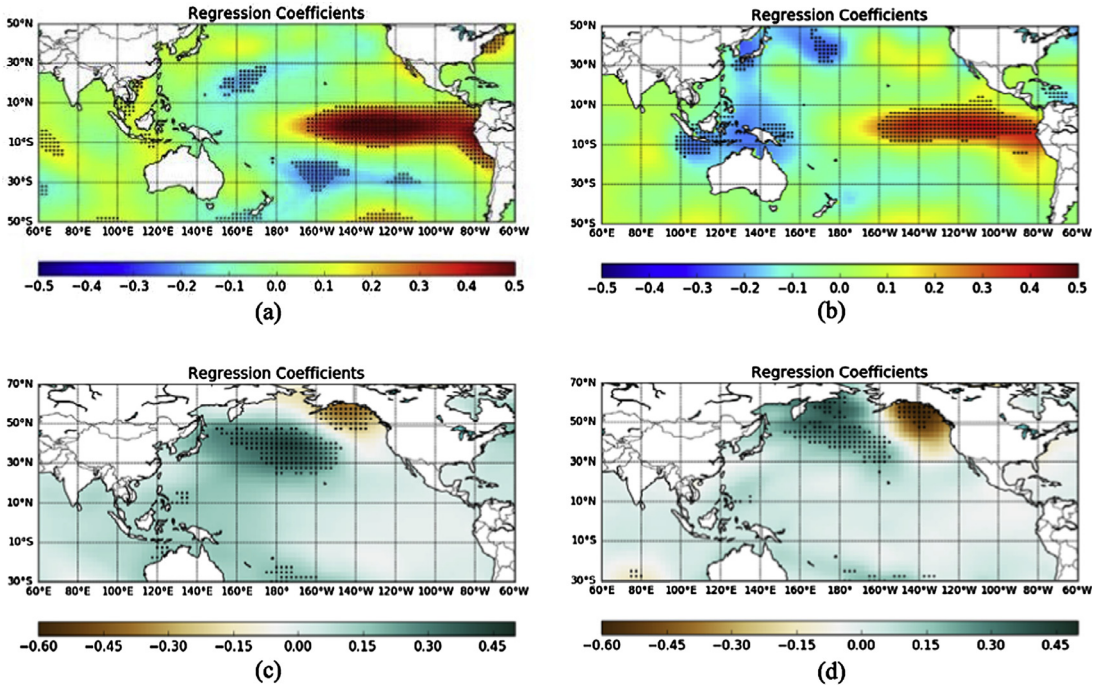

Fig. 5. Maps of SST (a), (b) and MSLP (c), (d) regressed on to December EOT of Rx5day (left) and total (right) precipitation.

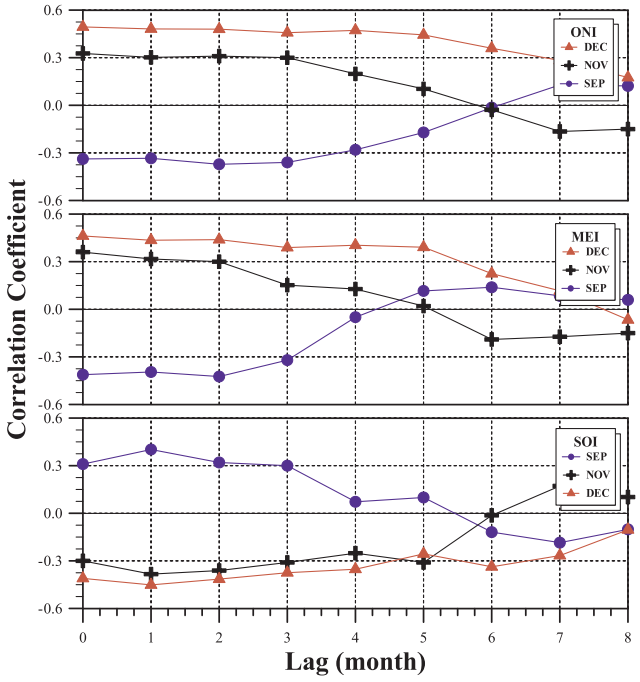

Fig. 6. Cross-correlation between climate indices and the leading monthly EOT.

monsoon variability. The monsoon indices show somewhat lower correlations with the leading EOT modes for Rx5day precipitation than those for total precipitation but exhibit a similar temporal pattern.

The monthly TCI indices were calculated for the index area to the south part of the Korean peninsula (Fig. 2). Each TCI is correlated with the EOT modes for Rx5day and total precipitation from May to November. As shown in Table 2, five EOTs show the significant correlation with the TCI time series, indicating that increased and decreased frequency of tropical cyclones passing through the index area is associated with enhanced and suppressed precipitation. The leading EOTs for September and October precipitation exhibit the strongest positive correlation with the tropical cyclone variability. This indicates that the leading EOT in fall season, located in eastern coastal area over the Korea peninsula, show significant positive correlation with the TCI. The general results from the above analysis are consistent with the findings investigated by Cha (2007), resulting in the significant correlation between tropical cyclones and seasonal precipitation patterns over the Korean peninsula.

4.3. Predictability of precipitation patterns

In addition to expanding our understanding of how CIs affect Korean precipitation variability, it is also of great importance to improve prediction capability of this variability. The previous correlation analysis did not take into account any time lag between the EOT time series for Rx5day and total precipitation and various CIs. If the CIs applied here have a significant impact on the precipitation anomaly over the Korean peninsula, then it is worthwhile to quantify the degree of this influence by a time-dependent cross-correlation analysis between the two time series that would be useful for forecasting purposes. To do this, we correlated the monthly EOTs for the Rx5day and total precipitation with CIs at monthly time lags of lag-0 month to lag-17 months, where the EOTs are lagging the CIs. The motivation to focus on the monthly time lag, e.g., a time interval of 0 to 17 months, is based on the fact that the climate signals used here are slowly evolving and this low-frequency behavior may provide substantial value as a long range predictor. The results of this analysis are presented in Table 3 as the cross-correlation coefficient values. The overall correlation coefficients are calculated at 0.01, 0.05 and 0.10 significance levels for better comparison.

The cross-correlation coefficient between ENSO and each EOT was computed for the ONI, the MEI, and the SOI. As shown in Table 3, the December EOT-1 exhibits significant positive correlations with the ONI time series up to the preceding June, while the September EOT-1 exhibits the negative correlations with the ONI up to the preceding June. The cross-correlation coefficient for the MEI time series provides qualitatively consistent behavior. Consistent with the above results, the December EOT-1 exhibits significant negative correlations with the SOI time series up to the preceding August, whereas the first EOT in

Table 3
Cross-correlation coefficients of the leading modes with climate indicators. The bold, single underlined bold, and double underlined bold indicate correlations that are statistically significant at the 0.10, 0.05, and 0.01 level. The plus indicates the following year.

Mode	CIs for Rx5day EOT modes							CIs for Total EOT modes						
Lag modes for Oceanic Nino Index (ONI)														
	JUN	JUL	AUG	SEP	OCT	NOV	DEC	JUN	JUL	AUG	SEP	OCT	NOV	DEC
SEP	-0.36	-0.37	-0.33	-0.34				-0.34	-0.38	-0.34	-0.41			
OCT	-0.17	-0.23	-0.22	-0.21	-0.18			-0.22	-0.30	-0.25	-0.24	-0.19		
NOV	0.10	0.20	0.30	0.31	0.30	0.33		0.25	0.32	0.34	0.35	0.34	0.39	
DEC	0.36	0.44	0.47	0.46	0.48	0.48	0.49	0.25	0.35	0.39	0.39	0.42	0.42	0.45
Lag modes for Multivariate ENSO Index (MEI)														
	JUN	JUL	AUG	SEP	OCT	NOV	DEC	JUN	JUL	AUG	SEP	OCT	NOV	DEC
SEP	-0.32	-0.42	-0.40	-0.41				-0.34	-0.39	-0.37	-0.44			
OCT	-0.12	-0.14	-0.15	-0.16	-0.15			-0.17	-0.16	-0.16	-0.18	-0.21		
NOV	0.02	0.13	0.15	0.30	0.32	0.36		0.22	0.28	0.26	0.34	0.40	0.45	
DEC	0.22	0.39	0.40	0.39	0.44	0.44	0.46	0.14	0.25	0.27	0.30	0.31	0.35	0.42
Lag modes for Southern Oscillation Index (SOI)														
	JUN	JUL	AUG	SEP	OCT	NOV	DEC	JUN	JUL	AUG	SEP	OCT	NOV	DEC
SEP	0.30	0.32	0.40	0.31				0.34	0.39	0.40	0.28			
OCT	0.28	0.01	0.12	0.02	0.02			0.34	0.04	0.11	0.04	0.11		
NOV	-0.31	-0.25	-0.31	-0.36	-0.38	-0.30		-0.39	-0.26	-0.34	-0.37	-0.39	-0.32	
DEC	-0.34	-0.26	-0.35	-0.37	-0.41	-0.45	-0.41	-0.10	-0.16	-0.30	-0.31	-0.30	-0.39	-0.49
Lag modes for Indian Ocean Dipole Index (IOD)														
	JUN	JUL	AUG	SEP	OCT	NOV	DEC	JUN	JUL	AUG	SEP	OCT	NOV	DEC
SEP	-0.29	-0.26	-0.30	-0.28				-0.31	-0.28	-0.26	-0.27			
OCT	0.09	-0.12	-0.19	-0.24	-0.17			-0.08	-0.21	-0.22	-0.06	-0.10		
NOV	-0.05	0.03	0.10	0.26	0.28	0.32		0.14	0.19	0.23	0.26	0.27	0.31	
DEC	0.20	0.16	0.22	0.21	0.25	0.22	0.09	0.07	0.06	0.09	0.09	0.11	0.14	-0.02

September shows a positive correlation with the SOI up to the preceding July. No significant correlation for the ENSO signal was detected during January to July reflecting the fact that relationships between the ENSO indicators and each EOT mode are generally not prominent at this time of year. The outcomes from the cross-correlation analysis above indicate that the teleconnected effects of the ENSO phenomena on the leading modes of Rx5day precipitation in the Korean peninsula are detectable at up to six-month lead time. Additionally, the leading EOTs for total precipitation also show significant lagged correlation with ENSO remote forcing as shown in Table 3. The ONI, MEI, and SOI from June to September (August to December) have significant negative (positive) correlations with the leading EOT for total precipitation in September (December). These CIs show slightly higher correlation coefficients with the Rx5day precipitation EOTs compared with the EOT modes for total precipitation, but both correlation results show a similar seasonal cycle. The above findings are consistent with the results reported by Lee and Julien (2017) who showed that the ENSO-related teleconnections to Korea resulted in drier than normal conditions during fall and wetter than normal conditions in winter season. Also, the non-linear precipitation response to ENSO in this study is similar to that found in Australia as described in King et al. (2014), Power et al. (2006), and Cai et al (2011).

The IOD is also associated with Rx5day and total precipitation variability in the Korean peninsula. In Table 3, the IOD from June to September has the negative correlations with the leading EOT for Rx5day and total precipitation in September, while the leading EOT modes for November precipitation show the positive correlation with September to November DMI indices. These findings show lower potential for predictability of the Rx5day and total precipitation in association with the IOD indicators compared to those of ENSO indices, reflecting the fact that the far reaching effects of the Indian Ocean SSTs on the East Asian climate variability are not strong compared to that of the Pacific Ocean SST due to their locations farther west over South Asia.

In addition to the cross-correlation analysis, the Pacific Ocean SSTs based on the ERSST.v4 dataset are regressed onto the EOTs with varying lead times to identify potential sources of predictability for monthly Rx5day and total precipitation. As shown in the Figs. 7 and 8, the above lag regressions of the Pacific Ocean SSTs onto September and December EOT-1 modes for Rx5day and total precipitation demonstrate that the leading EOTs show notable lagged and concurrent regression with strong ENSO signals over the equatorial Pacific. The December lag regression suggests noticeable predictability from the tropical Pacific Ocean SST with positive regression coefficients decreasing as the lag increases. The lagged regression signals continue until months prior to June at lag-6, and then the Pacific SST-related precipitation signals

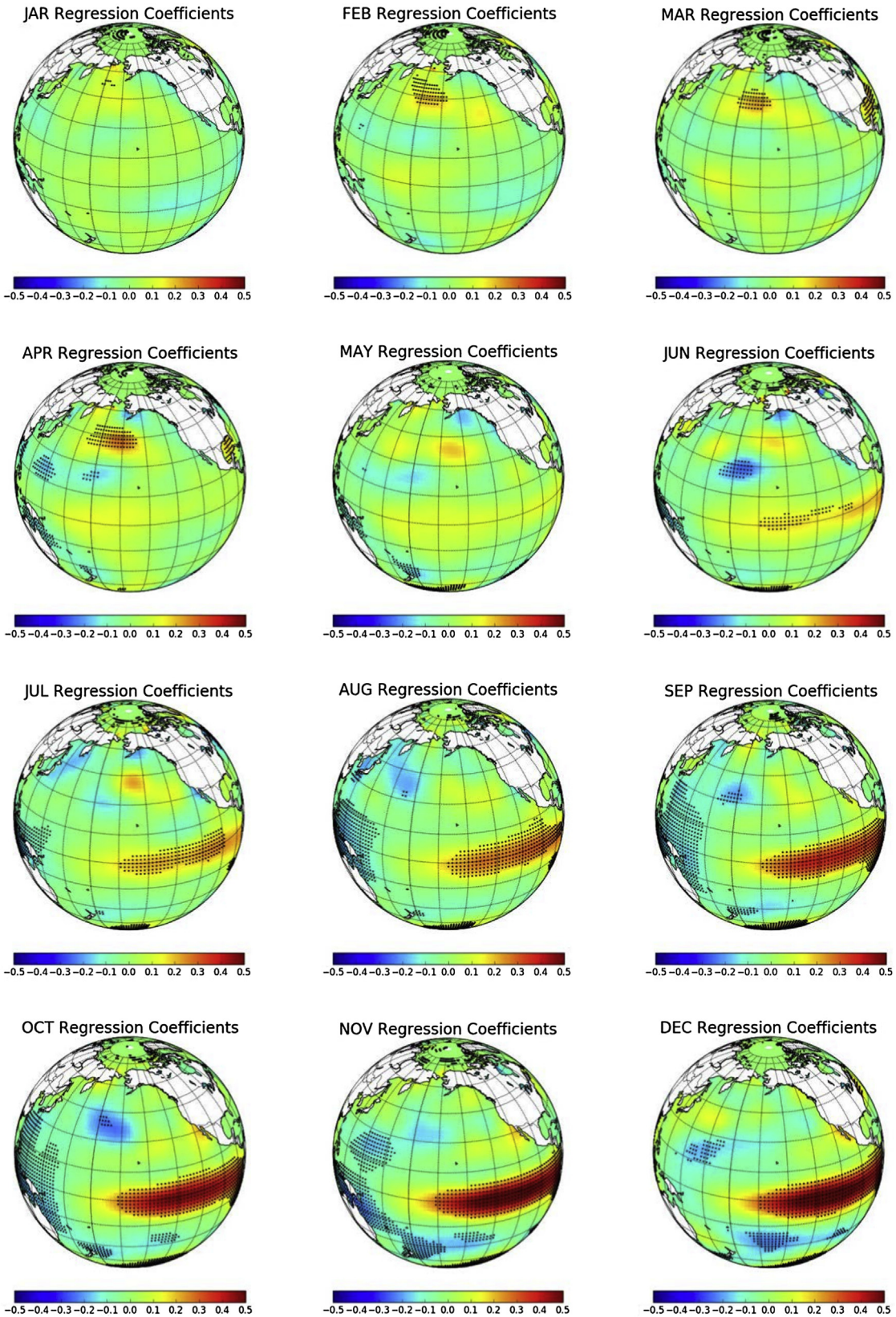

Fig. 7. Maps of SSTs of January to December regressed on to December Rx5day EOT1.

diminish. The September lag-0 to lag-3 regression representing regression June to September SSTs onto September EOT-1, indicates a negative correlation with tropical Pacific cold tongue SSTs. The negative signals extend to months prior to June at lag-3, and then do not exhibit substantial amplitude during January to May. Lag regression maps indicate coherent Pacific Ocean SST variability related to EOTs of Korean precipitation. Despite noise in the SST-precipitation relationship, the sources identified above may provide promise to improve prediction of

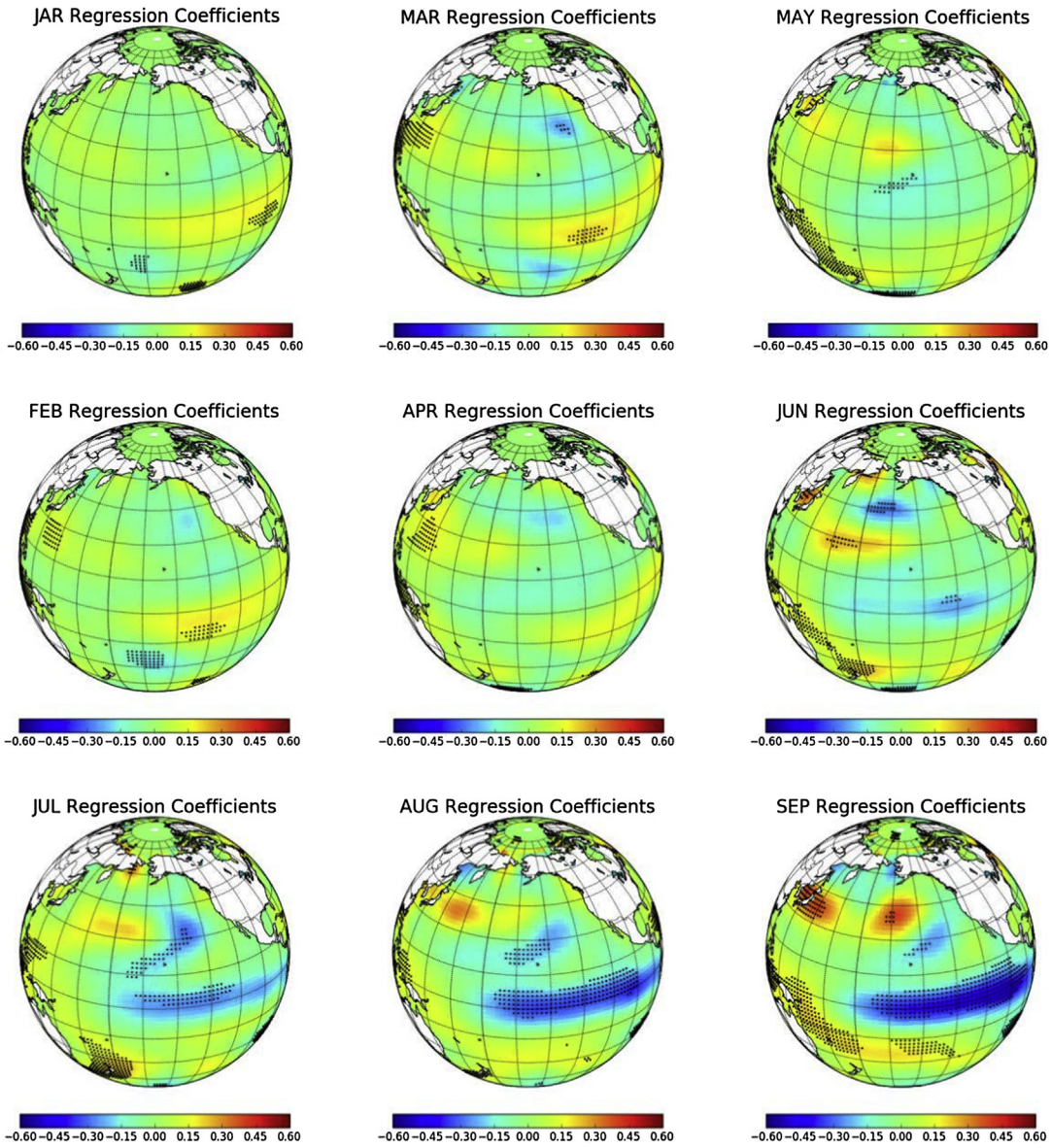

Fig. 8. Maps of SSTs of January to September regressed on to September Rx5day EOT1.

monthly precipitation variations over the Korean peninsula.

In December for extreme high and low precipitation, there is a different tendency in the ENSO-precipitation relationship. The lagged and concurrent SST regression onto the leading EOT-1 for extreme high and low precipitation anomalies in December account for the aforementioned different tendency as shown in Figs. 9 and 10. These lag-regression maps show that the regression coefficients of very wet extremes in December from Pacific SSTs are more evident than that of very dry December extremes. The lower predictability of January-April leading EOTs is attributed to weaker SST-precipitation relationships in this time of year. Consequently these findings of the potential sources of climate predictability indicate important implications for the seasonal forecasting the major hydrologic extremes such as flood and drought events.

5. Discussion

5.1. Spatiotemporal variability of precipitation

The spatiotemporal evolution of the leading EOT modes exhibits increasing trends during summer season and decadal variability for winter season. Ho et al. (2003) investigated long-term temporal change in the Korean peninsula by examining daily precipitation data over a period of 48 years from 1954 to 2001, and showed gradual increasing trend with time due to more frequent occurrences of extreme precipitation and increased cumulative precipitation. Also, in the super-ensemble prediction analysis, Kim et al. (2004) revealed that the time coefficients of the first two leading modes over the Korean peninsula exhibit significant decadal temporal cycles in winter precipitation patterns. These results are consistent with the outcomes of the current study that shows similar responses in Korean precipitation associated with tropical ENSO forcing. However, visual inspection of the station location maps in previous papers indicates that the significant relationships over the Korean peninsula were not sufficiently resolved due to the data coverage limitations. Our study resolves these issues through use of a high quality, high resolution Korean surface dataset, and also provides additional information on the CI-precipitation linkage over East Asia which was not identified in previous studies.

5.2. Teleconnection and predictability of EOTs and CIs

The EOT decomposition and cross-correlation analyses described in

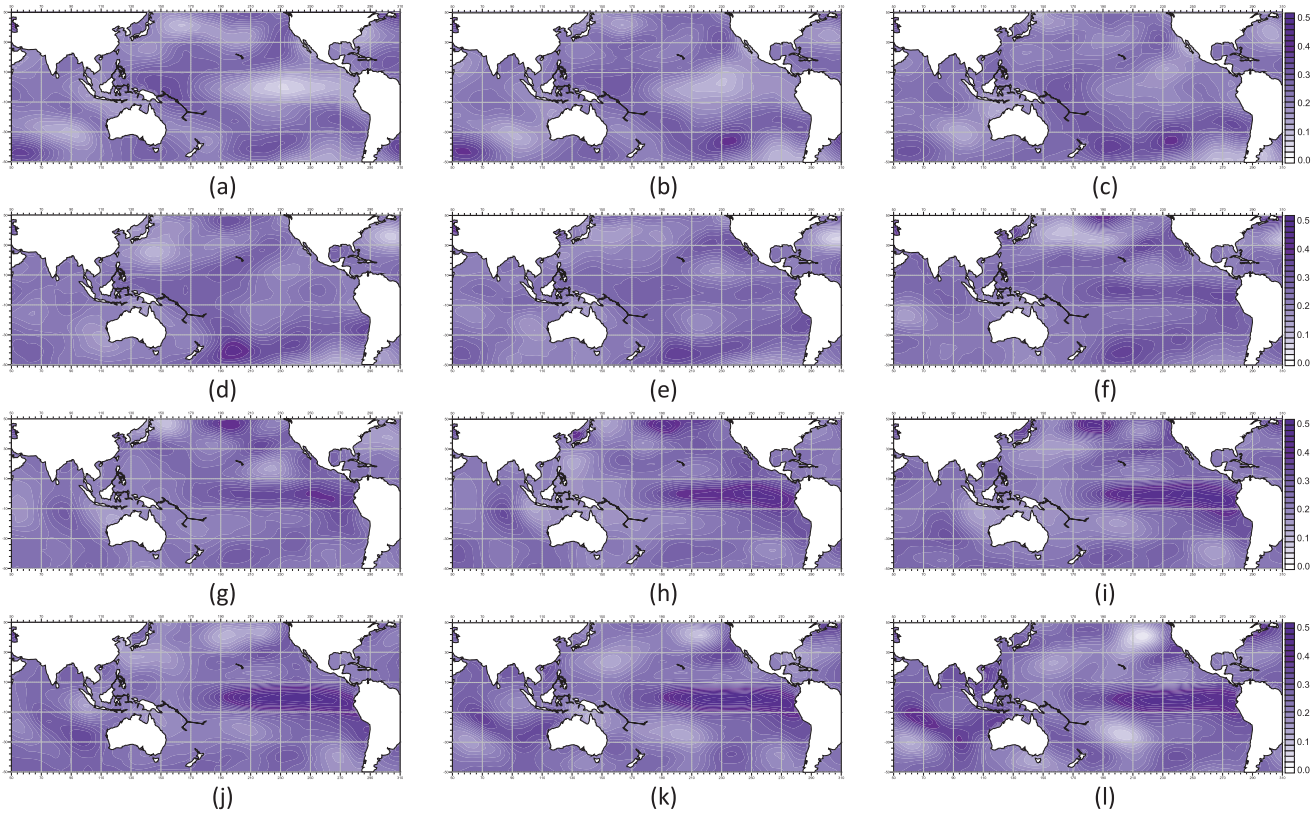

Fig. 9. Maps of SSTs from each calendar month (a)–(l) from January to December regressed on to December extreme EOT1for wetter-than-average December Rx5day values only.

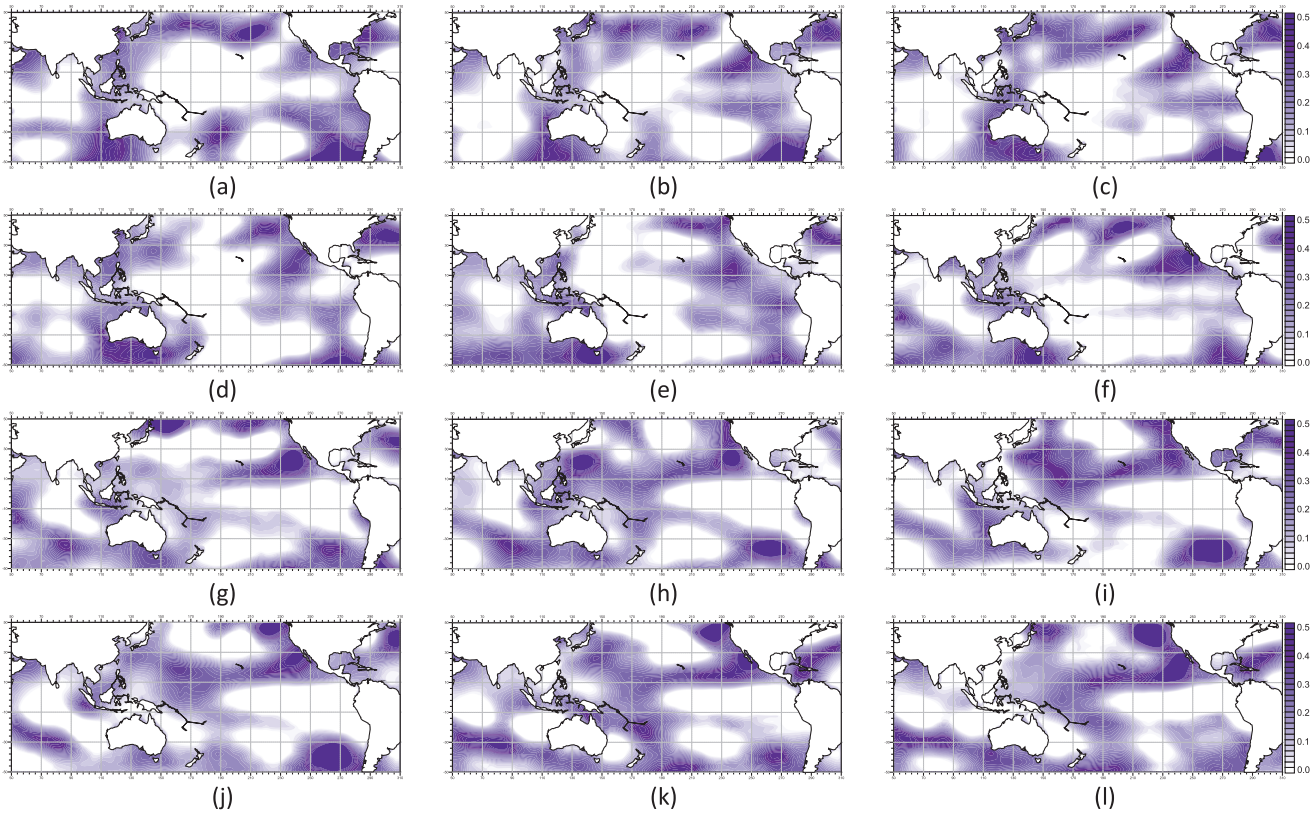

Fig. 10. As in Fig. 9, but for drier-than-average December Rx5day values only.

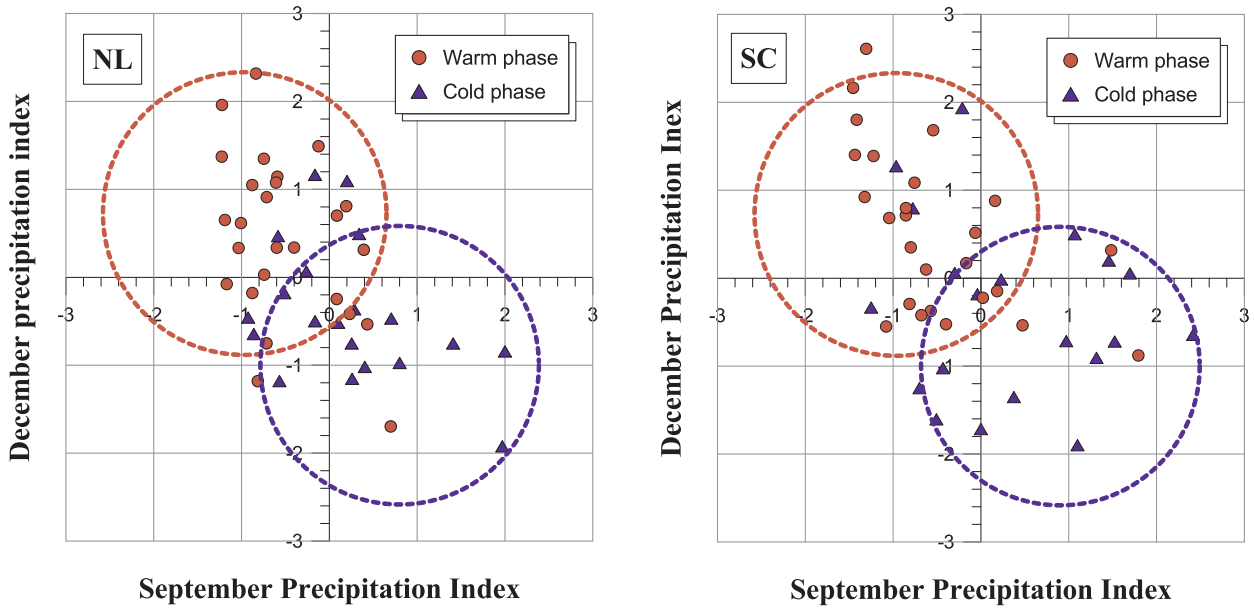

Fig. 11. The comparison of standardized indices for below (above) normal precipitation in September and above (below) normal precipitation in December during the warm (cold) phase of ENSO events using the monthly precipitation time series for north-inland (NL) mode (left) and south-coast (SC) mode (right).

the previous section demonstrate that leading mode of September precipitation has a negative correlation with the tropical thermal forcing over the Pacific Ocean, while that of December precipitation shows a positive correlation with the tropical Pacific SST variability. In other words, during the warm ENSO years below normal precipitation anomalies are observed in September, while above normal precipitation departures are observed in December. For the cold ENSO years, the opposite is true. Fig. 11 illustrates the comparison of standardized indices for below (above) normal precipitation in September and above (below) normal precipitation in December during the warm (cold) event years using the monthly precipitation data for both northern inland mode and southern coastal mode. The scatterplots for the warm phase are mostly distributed in the upper left part of the plot, while those for the cold phase are oppositely distributed in lower right part. These notable patterns for monthly precipitation data suggest that September and December are characterized by opposite signed tendency for an ENSO event of a given sign.

What causes the anomalous precipitation over the Korean Peninsula is explained by circulation anomalies associated with ENSO forcing based on composite difference of circulation fields. Northerly wind cut off the moisture supply from equator towards the Korean peninsula resulting in below-normal precipitation activity. In addition, the decline in September precipitation is caused by the depression of the second rainy period by reduction of the tropical storms and typhoons over East Asia during the warm phase years, while increase of precipitation in September of the cold phase years is in association with the intensification of the second rainy period resulting from more frequent occurrences of tropical cyclones. On the other hand, in November and December anomalous southwesterly wind prevails over the Korean peninsula and the northwestern part of the Philippine Sea anticyclone, reflecting damping phases of East Asia winter monsoon or a warmer than normal in winter. The anomalous southerly wind transports moist and warm air toward the Korean peninsula. This northward transport is attributed to a wetter than normal climate over the Korean peninsula.

The positive dipole mode of Indian Ocean favor heavy snow and lower surface temperature over the northern part of the Korean peninsula in Eastern Eurasia (Kripalani et al., 2010). The northerly winds are anomalously strong over that region and bring dry and cold air from the high latitudes to the Korean peninsula. Thus, the weak anomalous southerlies and the strong anomalous northerlies cut off the warm moisture supply towards the Korean peninsula causing below-normal precipitation activity. In contrast, the north Pacific subtropical high is slightly displaced north-westward in November southerly wind brings warm and wet air from the equator to the Korean peninsula. Thus, the strong anomalous southerlies will modulate the moisture supply towards the Korean peninsula leading to above-normal precipitation activity.

5.3. Comparison with previous studies

The overall results of the analyses presented here are in general agreement with those of other recent studies from the viewpoint of positive (negative) response during winter (fall) season, regarding the climatic impacts of the extreme phase of ENSO on hydroclimatic variables over the Korean peninsula. Cha (2007) examined the teleconnection between the remote ENSO forcing and Korean climate such as precipitation, atmospheric circulation, temperature, and so on, and revealed that the tropical ENSO forcing has a dominant impact on fluctuation of seasonal precipitation over South Korea modulating enhancement (suppression) of its magnitude. In addition, from a viewpoint of ENSO-precipitation signal seasons illustrated in the cross-correlation analysis for the leading modes of the Rx5day and total precipitation, the drier period of September is fairly coincident with the finding by Shin (2002) representing the suppression of early fall precipitation during the warm extreme event years. Therefore, it is apparent that the findings from this study are considered as an additional confirmation of aforementioned climatic far reaching effects of the large scale CIs on Korean precipitation variability, which indicate drier (wetter) conditions in early fall of the warm (cold) episode years and wetter (drier) conditions in winter of the extreme event years. Consequently, in the light of the preceding discussions, the overall outcomes from the present analyses provide further confirmative evidence of the significant climatic teleconnection between the large scale CIs and hydroclimatic variability over midlatitude.

6. Conclusions

In the current study, we apply an empirical orthogonal teleconnection (EOT) decomposition technique to Rx5day and total precipitation over the Korean peninsula to quantify the remote impacts of

large scale modes of climate variability as quantified through climate indices (CIs). We demonstrated the potential for prediction of these precipitation patterns based on knowledge of monthly tropical SST fields using cross-correlation and lag regression analyses for the leading EOT modes and ENSO and IOD indicators.

The spatiotemporal features of Rx5day and total precipitation over the Korean peninsula are dominated by a northern inland mode during summer and southern coastal mode in winter. The temporal evolution of the leading EOT modes exhibits an increasing trend during summer and an interdecadal oscillation for winter season. Both leading Rx5day and total precipitation modes show notable spatial homogeneity across the Korean peninsula during the summer seasons with widespread coherent precipitation patterns, while in the winter season, the only leading Rx5day EOT shows nationwide spatial homogeneity. The leading total precipitation EOT modes explain more of the variance in Korean precipitation variability than the leading Rx5day EOT modes. The ONI and MEI time series that explain tropical Pacific ENSO variability have significant negative correlations with the leading EOTs of Rx5day precipitation in June and September, whereas the leading EOTs for November and December exhibit positive correlations with the ONI and MEI time series. Consistent with these results, the SOI shows significant positive (negative) correlations with the first EOT mode for Rx5day precipitation during the boreal summer (winter). The three ENSO indicators generally show slightly higher correlation coefficients with the Rx5day precipitation EOTs compared with the EOT modes for total precipitation, but both correlation results show a similar seasonal cycle. The leading and second EOT modes of Rx5day and total precipitation are significantly positively correlated with the boreal fall IOD as quantified by the DMI index, while the two modes show a negative correlation with Indian Ocean SST anomalies in boreal winter. The leading EOTs for Rx5day and total precipitation also exhibit a significant positive correlation with an index of monsoon variability over the WNP region during November to December. The leading EOTs for September and October precipitation exhibit the strongest positive correlation with the tropical cyclone variability. From the results of cross-correlation and lag regression analyses, the leading EOTs for September and December Rx5day precipitation have predictability up to six months lead time from tropical Pacific SSTs, while a weak predictable response from Indian Ocean SSTs was detected at longer lead time. Also, the regression coefficients of the tropical Pacific SSTs onto very wet extremes in December are more evident than that for very dry December extremes.

References

Ashok, K., Guan, Z., Yamagata, T., 2001. Impact of the Indian Ocean Dipole on the relationship between the Indian monsoon rainfall and ENSO. Geophys. Res. Lett. 28, 4499–4502.

Ashok, K., Guan, Z., Yamagata, T., 2003. Influence of the Indian Ocean Dipole on the Australian winter rainfall. Geophys. Res. Lett. 30, 1821.

Bradley, R.S., Diaz, H.F., Kiladis, G.N., Eischeid, J.K., 1987. ENSO signal in continental temperature and precipitation records. Nature 327, 487–501.

Cai, W., Rensch, P.V., Cowan, T., 2011. Teleconnection pathways of ENSO and the IOD and the mechanisms for impacts on Australian rainfall. J. Clim. 24, 3910–3923.

Cha, E.J., 2007. El Niño-Southern Oscillation, Indian Ocean Dipole mode, a relationship between the two phenomena, and their impact on the climate over the Korean Peninsula. J. Korean Earth Sci. Soc. 28 (1), 35–44.

Daly, C., Neilson, P.R., Phillips, D.L., 1994. A statistical-topographic model for mapping climatological precipitation over mountainous terrain. J. Appl. Meteorol. 33, 140–158.

Daly, C., Halbleib, M., Smith, J.I., Gibson, W.P., Doggett, M.K., Taylor, G.H., Curtis, J., Pasteris, P.A., 2008. Physiographically sensitive mapping of temperature and precipitation across the conterminous United States. Int. J. Climatol. 28, 2031–2064.

Degefu, M.A., Bewket, W., 2017. Variability, trends, and teleconnections of stream flows with large-scale climate signals in the Omo-Ghibe River Basin, Ethiopia. Environ. Monitor. Assess. 189 (142), 1–22.

Douglas, A.E., Englehart, P.J., 1981. On a statistical relationship between autumn rainfall in the central equatorial pacific and subsequent winter precipitation in Florida. Mon. Weather Rev. 109, 2377–2382.

Ho, C.H., Lee, J.Y., Ahn, M.H., Lee, H.S., 2003. A sudden change in summer rainfall characteristics in Korea during the late 1970s. Int. J. Climatol. 23, 117–128.

Huang, B., Banzon, V.F., Freeman, E., Lawrimore, J., Liu, W., Peterson, T.C., Smith, T.M., Thorne, P.W., Woodruff, S.D., Zhang, H.M., 2014. Extended Reconstructed Sea Surface Temperature version 4 (ERSST.v4): Part I. Upgrades and intercomparisons. J. Clim. https://doi.org/10.1175/JCLI-D-14-00006.1.

Kahya, E., Dracup, J.A., 1994. The influences of Type 1 El Niño and La Niña events on streamflows in the Pacific southwest of the United States. J. Clim. 7, 965–976.

Karabörk, M.Ç., Kahya, E., 2003. The teleconnections between extreme phases of Southern Oscillation and precipitation patterns over Turkey. Int. J. Climatol. 23, 1607–1625.

Kim, J.S., Li, R.C.Y., Zhou, W., 2012. Effects of the Pacific-Japan teleconnection pattern on tropical cyclone activity and extreme precipitation events over the Korean Peninsula. J. Geophys. Res. 117, D18109. https://doi.org/10.1029/2012JD017677.

Kim, M.K., Kang, I.S., Park, C.K., Kim, K.M., 2004. Super ensemble prediction of regional precipitation over Korea. Int. J. Climatol. 24, 777–790.

King, A.D., Klingaman, N.P., Alexander, L.V., Donat, M.G., Jourdain, N.C., Maher, P., 2014. Extreme rainfall variability in Australia: Patterns, drivers, and predictability. J. Clim. 27, 6035–6050.

Klingaman, N.P., Woolnough, S.J., Syktus, J., 2013. On the drivers of inter-annual and decadal rainfall variability in Queensland, Australia. Int. J. Climatol. 33, 2413–2430.

Kiladis, G.N., Diaz, H.F., 1989. Global climatic anomalies associated with extremes in the Southern Oscillation. J. Clim. 2, 1069–1090.

Knapp, K.R., Kruk, M.C., Levinson, D.H., Diamond, H.J., Neumann, C.J., 2010. The international best track archive for climate stewardship (ibtracs): Unifying tropical cyclone best track data. Bull. Am. Meteorol. Soc. 91, 363–376.

Kripalani, R.H., Oh, J.H., Chaudhari, H.S., 2010. Delayed influence of the Indian Ocean Dipole mode on the East Asia-West Pacific monsoon: possible mechanism. Int. J. Climatol. 30, 197–209.

Kug, J.S., Ahn, M.S., Sung, M.K., Yeh, S.W., Min, H.S., Kim, Y.H., 2010. Statistical relationship between two types of El Niño events and climate variation over the Korean Peninsula. Asia-Pacific J. Atmos. Sci. 45 (4), 467–474.

Lee, J.H., Julien, P.Y., 2015. ENSO impacts on temperature over South Korea. Int. J. Climatol. 10 1002/4581.

Lee, J.H., Julien, P.Y., 2016. Teleconnections of the ENSO and South Korean precipitation patterns. J. Hydrol. 534, 237–250.

Lee, J.H., Julien, P.Y., 2017. Influence of the El Niño/Southern oscillation on South Korean streamflow variability. Hydrol. Process. 10 1002/hyp. 11168.

Mehr, A.D., Nourani, V., Hrnjica, B., Molajou, A., 2017. A binary genetic programing model for teleconnection identification between global sea surface temperature and local maximum monthly rainfall events. J. Hydrol. 555, 397–406.

Moon, Y.I., Kwon, H.H., Kim, D.K., 2005. A study of relationships between the sea surface temperatures and rainfall in Korea. J. KWRA 38 (12), 995–1008.

Nourani, V., Sattari, M.T., Molajou, A., 2017. Threshold-based hybrid data mining method for long-term maximum precipitation forecasting. Water Resour. Manage. 1–14.

Power, S.B., Haylock, M., Colman, R., Wang, X., 2006. The predictability of Interdecadal changes in ENSO activity and ENSO teleconnection. J. Clim. 19, 4755–4771.

Price, C., Stone, L., Huppert, A., Rajagopalan, B., Alpert, P., 1998. A possible link between El Niño and precipitation in Israel. Geophys. Res. Lett. 25, 3963–3966.

Rasmusson, E.M., Wallace, J.M., 1983. Meteorological aspects of the El Niño/southern oscillation. Science 222, 1195–1202.

Redmond, K.T., Koch, R.W., 1991. Surface climate and streamflow variability in the western United States and their relationship to large circulation indices. Water Resour. Res. 27 (9), 2381–2399.

Ropelewski, C.F., Halpert, M.S., 1989. Precipitation patterns associated with the high index phase of the southern oscillation. J. Clim. 2, 268–284.

Saji, N.H., Goswami, B.N., Vinayachandran, P.N., Yamagata, T., 1999. A dipole mode in the tropical Indian Ocean. Nature 401, 360–363.

Shin, H.S., 2002. Do El Niño and La Niña have influences on South Korean hydrologic properties? In: Proceedings of the 2002 Annual Conference, Japan Society of Hydrology and Water Resources, pp. 276–282.

Shukla, J., Paolino, D.A., 1983. The southern oscillation and long-range forecasting of summer monsoon rainfall over India. Mon. Weather Rev. 111, 1830–1837.

Smith, I.N., 2004. An assessment of recent trends in Australian rainfall. Aust. Meteor. Mag. 53, 163–173.

Van den Dool, H.M., Saha, S., Johansson, Å., 2000. Empirical orthogonal teleconnections. J. Clim. 13, 1421–1435.

Walker, G.T., 1923. Correlation in seasonal variations of weather, V III, A preliminary study of world weather. Mem. Indian Meteorol. Dep. 24, 75–131.

Wang, B., Wu, R., Fu, X., 2000. Pacific-East Asian teleconnection: how does ENSO affect east Asian climate. J. Clim. 13, 1517–1536.

Wang, B., Wu, R., Li, J., Liu, J., Chang, C., Ding, Y., Wu, G., 2008. How to measure the strength of the East Asian Summer Monsoon. J. Clim. 1175.

Yeh, S.W., Cai, W., Min, S.K., Mcphaden, M.J., Dommenget, D., Dewitte, B., Collins, M., Ashok, K., An, S.I., Yim, B.Y., Kug, J.S., 2017. ENSO atmospheric teleconnections and their response to greenhouse gas forcing. Rev. Geophys. 2018. https://doi.org/10.1002/2017RG000568.